

Rapid Gaussian Boson Sampling Circuit Screening for GKP States Creation via a Two-Stage Machine Learning Surrogate

Mohammad Amin Khanpour¹ and Hossein Davoodi Yeganeh^{a2,3}

¹*Department of Physics, Shahid Beheshti University, Tehran, Iran*

²*AriaQuanta Quantum Computing Center, Tehran, Iran*

³*Quantum Research Center, Shahid Sattari University of Aeronautical Sciences and Technology, Tehran, Iran*

Gottesman–Kitaev–Preskill (GKP) states are essential non-Gaussian resources for fault-tolerant photonic quantum computing, enabling logical qubit encoding with intrinsic robustness against errors. Several approaches to GKP state preparation have been explored, including measurement-based protocols in circuit QED and trapped-ion systems, cat-state breeding, and photon-subtraction schemes. However, these methods are either restricted to specific platforms or require deep non-Gaussian resource chains with exponentially low success probabilities. Gaussian Boson Sampling (GBS) offers a compelling all-photonic alternative by generating non-Gaussian states through measurement-induced nonlinearity, without the need for matter-based ancilla or active feedforward. Nevertheless, its practical implementation is limited by the exponential computational cost of evaluating matrix hafnians— $\#P$ -complete functions that govern photon-number probabilities. To address this challenge, we introduce a two-stage Histogram Gradient Boosting surrogate pipeline that predicts, without any hafnian computation, the optimal heralding pattern, circuit fidelity, and post-selection probability for candidate GBS circuits, while reserving exact quantum simulation exclusively for surrogate-selected candidates. Trained on circuit configurations across 3–5 optical modes, the surrogate achieves 90.0% GKP-detection accuracy on a held-out set, representing a 23.7 percentage-point improvement over the baseline, with a fidelity mean absolute error of 0.032 and a log-scale post-selection probability $R^2 = 0.837$, reducing the total simulation burden by approximately 90%.

Keywords: GKP states; Gaussian boson sampling; machine learning surrogates; fault-tolerant quantum computing.

I. INTRODUCTION

Quantum computation promises solutions to classically intractable problems in cryptography, optimisation, and simulation. However, realising this potential requires hardware capable of performing high-fidelity operations at scale [1]. Among the physical platforms currently under development, photonic quantum computing has emerged as a particularly promising candidate due to its room-temperature operation, low decoherence, and natural compatibility with quantum communication infrastructure [2, 3]. A central challenge in the development of practical photonic quantum processors is the generation of non-Gaussian resource states, among which Gottesman–Kitaev–Preskill (GKP) states play a central role [4]. GKP states encode a logical qubit within a single bosonic mode in a way that is intrinsically resilient to small displacement errors in both quadratures. Moreover, they are fully compatible with Gaussian operations such as beamsplitters, squeezers, and phase rotations, which are naturally implemented in photonic hardware. When supplemented with GKP magic states, this framework enables universal fault-tolerant quantum computation [5–7], thereby making the preparation of GKP states a key requirement for scalable photonic quantum processors. The generation of GKP states remains a nontrivial task. Ideal GKP states require infinite squeezing and are therefore unphysical; in practice, finite-energy approximations must be prepared with sufficiently high fidelity, typically on the order of $F \geq 0.90$ with respect to the target finite-energy GKP state [6, 8], in order to provide meaningful protection against logical errors. Several approaches to GKP state preparation have been investigated. Measurement-based schemes in circuit QED and trapped-ion platforms have shown promising performance [9–11], but they are inherently tied to matter-based architectures and are therefore not directly compatible with fully photonic implementations. Cat-state breeding and photon-subtraction techniques are fully optical and hardware-compatible; however, they typically require long sequences of non-Gaussian operations, which results in exponentially suppressed success probabilities [12, 13]. Iterative protocols offer a more structured route toward target state generation, but they rely on real-time adaptive feedforward, introducing substantial experimental overhead and implementation complexity [14]. In contrast, Gaussian boson sampling (GBS) [15–18] provides a fully photonic alternative. In this approach, a multimode Gaussian optical circuit—comprising squeezed-state sources, a linear interferometer, and photon-number-resolving (PNR) detectors—generates non-Gaussian states through measurement-induced nonlinearities, without the need for matter-based ancilla systems or active feedforward control. When specific heralded photon-number

^a corresponding author: h.yeganeh@ariaquanta.com, h.yeganeh@ssau.ac.ir

patterns are post-selected across all but one output mode, the remaining mode is projected into a non-Gaussian state that can closely approximate the target GKP wavefunction. The central engineering challenge is therefore to jointly determine the circuit parameters—namely squeezing amplitudes, interferometer angles and phases—and the appropriate heralding pattern, while simultaneously satisfying the dual constraints of high state fidelity and a sufficiently high post-selection probability. The evaluation of a single GBS circuit configuration is computationally expensive, as photon-number probabilities are expressed in terms of matrix hafnians [19, 20], which are #P-complete functions that scale exponentially with photon number. For circuits with a Fock-space truncation of $n_{\max} = 12$ and five modes, a single evaluation requires approximately five minutes on a modern workstation. As a result, systematic exploration of the parameter space—requiring thousands of such evaluations—becomes computationally intractable without efficient approximation methods or surrogate models. This bottleneck motivates the use of surrogate modelling: a learned function that approximates the mapping from circuit parameters to performance metrics at a computational cost orders of magnitude lower than that of exact simulation [21]. Such models enable rapid screening during parameter-space exploration, while restricting exact simulations to the final validation of the most promising candidates. This paper presents the *GKP Circuit ML Pipeline v2*, a two-stage gradient-boosted surrogate framework designed to address the circuit screening problem in a systematic manner. At its core, a machine learning surrogate is a data-driven approximation of an expensive simulation function, trained on precomputed input–output pairs to learn the mapping from circuit parameters to performance metrics at a computational cost that is several orders of magnitude lower than that of the original simulator. The surrogate developed in this work—based on `HistGradientBoosting` models from `scikit-learn`—learns this mapping from 689 pre-optimised GBS circuit configurations, each annotated with ground-truth fidelity and post-selection probability obtained via exact quantum simulation. At inference time, it predicts the optimal heralding pattern, circuit fidelity, and post-selection probability for a new candidate circuit in approximately 1–5 ms, without requiring any hafnian computations. The pipeline architecture is guided by three design principles that distinguish it from a straightforward application of off-the-shelf regression methods. First, it adopts a cascade structure: a Stage 1 `HistGradientBoostingClassifier` predicts the optimal heralding pattern directly from circuit parameters, while Stage 2 regressors condition their predictions of fidelity and post-selection probability on this inferred pattern, thereby explicitly leveraging the physical dependence between herald photon-number structure and achievable output-state quality. Second, it incorporates a physics-informed feature representation that augments the raw circuit parameters with eleven domain-derived aggregate statistics, capturing aspects such as total squeezing strength, interferometer coupling uniformity, and phase coherence. This representation allows a single fixed-dimensional model to generalise across circuits with varying mode counts without requiring topology-specific retraining. Third, and most importantly for experimental robustness, the surrogate is not used in isolation: every circuit it identifies as GKP-capable ($F \geq 0.90$) is subsequently validated using full exact quantum simulation via Strawberry Fields [22] and `thewalrus` [20], yielding confirmed values of fidelity, post-selection probability, Wigner function, and Wigner logarithmic negativity. This conditional validation strategy effectively turns the surrogate into a computational gating mechanism, which filters candidate circuits prior to expensive simulation rather than replacing it entirely. This distinction becomes particularly important when the model is applied outside its training distribution, as highlighted by the systematic failure cases discussed in Section V. The pipeline is trained on 689 pre-simulated circuit configurations spanning 3–5 optical modes, Fock-space truncations of $n_{\max} \in \{4, 8, 12\}$, and target squeezing levels $\Delta \in \{3\text{--}11\}$ dB. Evaluation is performed on a 170-sample holdout set and further stress-tested on nine representative circuits, including two deliberately constructed failure cases designed to probe the surrogate’s distributional limits. The study also provides a candid characterization of the pipeline’s limitations, including a systematic failure mode associated with squeezing-parameter sign conventions outside the training distribution, as well as a cascade vulnerability stemming from the 36% misclassification rate of the Stage 1 pattern predictor. Section II introduces the necessary background on GKP states, Gaussian boson sampling (GBS) circuit architectures, and the computational complexity of the hafnian. Section III details the pipeline design, dataset construction, feature engineering, and model architecture. Section IV presents quantitative results, while Section V provides case-by-case comparisons between surrogate predictions and full quantum simulations. Finally, Section VI discusses limitations and potential mitigation strategies, and Section VII concludes the paper.

II. BACKGROUND

A. GKP States

GKP states encode a logical qubit in the infinite-dimensional Hilbert space of a single harmonic oscillator by distributing logical codewords over a periodic lattice in phase space [4, 23]. The central physical idea is that logical information is stored in the *periodicity* of the wavefunction rather than in any single degree of freedom, which makes the encoding naturally robust against small phase-space displacements. In particular, displacements smaller than

$\sqrt{\pi}/2$ in either quadrature can be corrected via syndrome measurements without destroying the encoded logical state.

This structure differs fundamentally from discrete-variable error-correcting codes: the correctable error set is continuous rather than discrete, and protection arises from the geometric regularity of the phase-space lattice rather than from Hamming distance between codewords. To formalise this construction, the square-lattice encoding defines the logical computational basis states $|\mu\rangle_L$ for $\mu \in \{0, 1\}$ as stabilised by the Weyl–Heisenberg displacement operators:

$$S_q = \exp(i 2\sqrt{\pi} \hat{q}), \quad S_p = \exp(-i 2\sqrt{\pi} \hat{p}). \quad (1)$$

These stabilisers enforce a periodic phase-space structure, rendering the code intrinsically robust to small displacement errors in both quadratures [24, 25].

Since ideal GKP states require infinite squeezing and are therefore unphysical, practical implementations rely on finite-energy approximations characterised by an envelope parameter Δ , which governs the trade-off between state fidelity and physical normalisability. The finite-energy logical codewords can be written as

$$|\mu\rangle_L \propto \hat{E}_L |\mu\rangle_{\text{ideal}}, \quad (2)$$

where $\hat{E}_L = \exp(-\Delta^2 \hat{n})$ denotes a Gaussian envelope operator acting on Fock space [26]. In this formulation, larger values of Δ correspond to a tighter localisation of the state in phase space and a closer approximation to the ideal codeword, at the expense of an increased mean photon number.

The fidelity between a finite-energy approximation and the ideal codeword increases monotonically with Δ ,

$$F(\Delta) \xrightarrow{\Delta \rightarrow \infty} 1, \quad \text{monotonically.} \quad (3)$$

In the Fock basis, the logical state $|0\rangle_L$ has support only on even photon-number eigenstates:

$$|0\rangle_L = \sum_k c_{2k} |2k\rangle, \quad (4)$$

where the coefficients c_{2k} satisfy the normalisation condition $\sum_k |c_{2k}|^2 = 1$. In practice, these coefficients are obtained via numerical diagonalisation of the finite-energy GKP Hamiltonian,

$$H_{\text{GKP}} = -\cos(2\sqrt{\pi} \hat{q}) - \cos(2\sqrt{\pi} \hat{p}), \quad (5)$$

which enforces the underlying phase-space lattice structure [26].

Similarly, the logical state $|1\rangle_L$ is supported exclusively on odd Fock states:

$$|1\rangle_L = \sum_k c_{2k+1} |2k+1\rangle. \quad (6)$$

This parity structure—restricting $|0\rangle_L$ to even photon numbers and $|1\rangle_L$ to odd photon numbers—has direct implications for circuit design, since valid heralding patterns must respect this symmetry. The fidelity between a prepared state $|\psi\rangle$ and a target finite-energy codeword $|\mu\rangle_L$ is defined as

$$F = |{}_L\langle \mu | \psi \rangle|^2. \quad (7)$$

A fidelity threshold of $F \geq 0.90$ is commonly regarded as necessary—though not sufficient—for practical fault-tolerant operation [8].

State quality is further quantified using the Wigner logarithmic negativity (WLN):

$$\text{WLN} = \log \left(\iint |W(q, p)| dq dp \right). \quad (8)$$

A positive WLN ($\text{WLN} > 0$) is a necessary, though not sufficient, condition for quantum computational advantage beyond what is classically simulable using Gaussian methods [27]. Importantly, a state may satisfy $F \geq 0.90$ relative to a GKP target while still exhibiting $\text{WLN} \approx 0$, in which case it remains classically simulable and provides no meaningful advantage for fault-tolerant quantum computation.

B. Gaussian Boson Sampling and GKP State Generation

Gaussian boson sampling (GBS) provides an all-photon mechanism for generating non-Gaussian states via measurement-induced nonlinearity, without the need for matter-based ancilla systems or active feedforward [15]. The central idea is as follows: a multimode Gaussian state—prepared using single-mode squeezers and evolved through a passive linear interferometer—is measured with photon-number-resolving (PNR) detectors on all but one output mode.

By post-selecting on a specific heralding pattern $\mathbf{m} = (m_1, m_2, \dots, m_{n_{\text{modes}}-1})$ across the measured modes, the remaining unmeasured mode is projected into a conditional non-Gaussian state that is fully determined by the circuit parameters and the chosen herald outcome. By appropriately tuning the squeezing amplitudes and interferometer angles, this conditional state can be engineered to approximate a target GKP wavefunction with high fidelity.

The probability of observing a given herald pattern, denoted $p(\mathbf{m})$, determines the rate at which usable resource states are produced. This introduces an intrinsic trade-off between state fidelity and preparation efficiency, which motivates the surrogate-based optimisation framework developed in this work.

Formally, Gaussian boson sampling (GBS) can be described as follows. A multimode Gaussian state, characterised by its covariance matrix Σ and displacement vector $\boldsymbol{\mu}$, is transformed through a passive linear optical circuit and subsequently measured. The resulting photon-number statistics are determined by hafnians of submatrices of the transformed covariance matrix, rendering exact classical simulation widely believed to be computationally intractable [16, 19, 28].

In the context of state preparation, the post-selection probability associated with a herald pattern \mathbf{m} in an ideal lossless circuit is given by

$$p(\mathbf{m}) \propto \frac{|\text{Haf}(A_{\mathbf{m}})|^2}{\prod_i m_i!}, \quad (9)$$

where $A_{\mathbf{m}}$ denotes the submatrix of the covariance structure selected by the pattern and the underlying circuit parameters.

In this setting, valid herald patterns are those satisfying $\sum_i m_i = n_{\text{max}}$, with each entry being a non-negative integer, $m_i \geq 0$, across the $n_{\text{modes}} - 1$ measured modes.

C. The Hafnian and Computational Complexity

The hafnian of a $2n \times 2n$ symmetric matrix A is defined as

$$\text{Haf}(A) = \sum_{\sigma \in \text{PMP}(2n)} \prod_{(i,j) \in \sigma} A_{ij}, \quad (10)$$

where the sum runs over all perfect matchings of $2n$ elements. This quantity is #P-hard to evaluate [19], and is therefore at least as computationally difficult as counting the solutions to an NP problem. The best known classical algorithms scale as $\mathcal{O}(2^n \cdot n^2)$, which restricts exact evaluation to relatively small system sizes. In practice, the `thewalrus` library implements highly optimised C++ routines with symmetry-based accelerations, although the underlying exponential scaling remains unchanged.

The practical implications for GKP circuit design are significant. For five-mode circuits with $n_{\text{max}} = 12$, a single evaluation of a (circuit configuration, herald pattern) pair requires approximately five minutes on a modern workstation using optimised routines from the `thewalrus` library [20]. Given up to 15 valid herald patterns in this setting, exhaustive evaluation of a single circuit therefore requires roughly 75 minutes. As a result, screening 1,000 candidate configurations would amount to approximately 1,250 CPU-hours, making brute-force exploration impractical for interactive design or large-scale optimisation. Even for smaller instances such as $n_{\text{max}} = 8$ with four modes, individual evaluations still require on the order of 10–30 seconds, which remains prohibitive for extensive search.

The surrogate pipeline circumvents this bottleneck by reducing screening time to milliseconds per circuit, while restricting expensive quantum simulations to those candidates that are predicted to be GKP-capable.

D. GBS Circuit Architecture

The GBS circuit studied in this work follows the architecture established in [29] and is implemented using the Strawberry Fields quantum photonics library [22]. It consists of three stages.

Stage 1 – Single-mode squeezing. Each of the n_{modes} input vacuum modes is prepared in a squeezed state using $\text{Sgate}(r_k, 0)$, where r_k is the squeezing amplitude (related to squeezing in dB by $r = \ln(10) \times \text{dB}/20$). Squeezing amplitudes are optimised within $r_k \in [-r_{\text{max}}, r_{\text{max}}]$, where r_{max} corresponds to 15 dB.

Stage 2 – Linear interferometer. A rectangular Clements-decomposition interferometer [30] transforms the squeezed product state into a multimode entangled Gaussian state. It consists of $n_{\text{modes}}(n_{\text{modes}} - 1)/2$ beamsplitter gates $\text{BSgate}(\theta_k, \phi_k)$, where $\theta_k \in [-\pi, \pi]$ is the mixing angle and $\phi_k \in [-\pi, \pi]$ is the relative phase. The Clements architecture guarantees universality: any passive linear-optical unitary $U \in U(n_{\text{modes}})$ can be realised by appropriate choice of these parameters.

Stage 3 – Photon-number-resolving measurement and post-selection. The output modes of the interferometer are directed to photon-number-resolving (PNR) detectors. Post-selection is applied to the first $n_{\text{modes}} - 1$ output modes: only measurement outcomes matching the target herald pattern $\mathbf{m} = (m_1, m_2, \dots, m_{n_{\text{modes}}-1})$ are accepted. Conditioned on this outcome, the remaining undetected output mode is projected into a non-Gaussian heralded state whose structure is entirely determined by the circuit parameters and the specific pattern. The post-selection probability $p(\mathbf{m})$, governed by the hafnian of the relevant covariance submatrix (Eq. (9)), sets the rate at which usable resource states are produced. All simulations in this work are performed in the lossless idealisation ($T_k = 1$ at all points in the circuit), so the heralded output is a pure state; the code infrastructure supports optional loss channels at multiple circuit locations, but these are not employed in the results reported here.

The total number of free circuit parameters is:

$$n_{\text{params}} = n_{\text{modes}} + n_{\text{modes}}(n_{\text{modes}} - 1), \quad (11)$$

giving 9, 16, and 25 parameters for three-, four-, and five-mode circuits respectively.

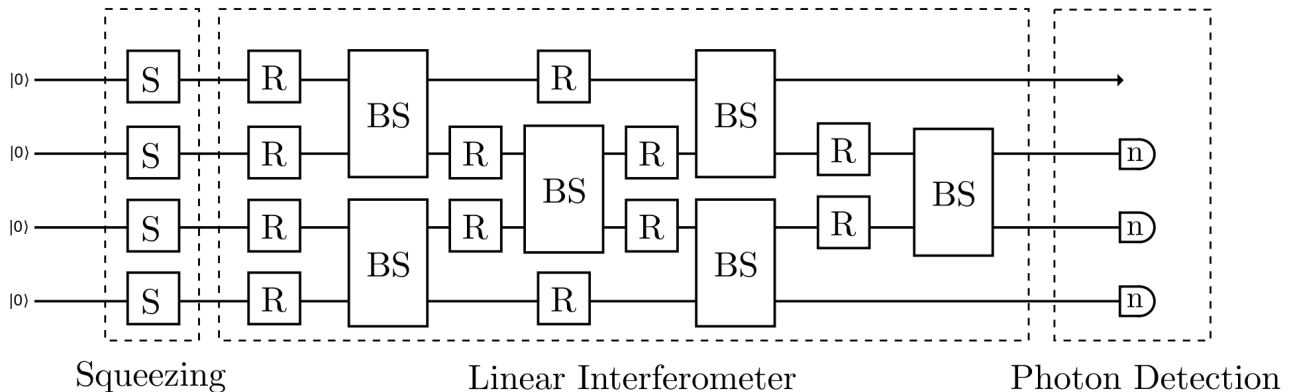


FIG. 1. GBS circuit schematic for GKP state preparation. The circuit consists of (left to right): single-mode squeezing gates on all n_{modes} input modes, a rectangular Clements beamsplitter interferometer, photon-number-resolving (PNR) detectors post-selecting on herald pattern $\mathbf{m} = (m_1, \dots, m_{n_{\text{modes}}-1})$ on the first $n_{\text{modes}} - 1$ modes, and the undetected output mode which collapses into the heralded GKP state.

III. METHODS

A. Pipeline Overview

The GKP Circuit ML Pipeline v2 is distinguished from a naive surrogate approach by four structural features that reflect the underlying physics of the problem. First, it employs a *cascade architecture*: Stage 1 predicts the optimal heralding pattern directly from circuit parameters, while Stage 2 conditions its predictions of fidelity and post-selection probability on the Stage 1 output. This design explicitly leverages the dependence of achievable fidelity on the specific photon-number configuration being post-selected, reformulating the task as conditionally structured rather than fully joint multivariate regression. Second, the feature representation augments raw circuit parameters with eleven physics-inspired summary statistics that encode prior knowledge about squeezing distributions, interferometer coupling structure, and phase coherence. This enables generalisation across circuits of varying size within a unified fixed-dimensional representation. Third, and most importantly from an experimental standpoint, the surrogate is not used as a standalone predictor. Any circuit classified as GKP-capable ($F \geq 0.90$) is subsequently validated via full quantum simulation using Strawberry Fields [22] and `thelrus` [20], producing verified estimates of fidelity, success

probability, Wigner function, and Wigner logarithmic negativity. In this way, the surrogate acts as a computational gating mechanism rather than a replacement for simulation. Fourth, the study provides a detailed characterisation of failure modes, including a systematic error arising from squeezing-parameter sign conventions outside the training distribution, as well as a cascade-level vulnerability associated with the 36% misclassification rate of the Stage 1 classifier.

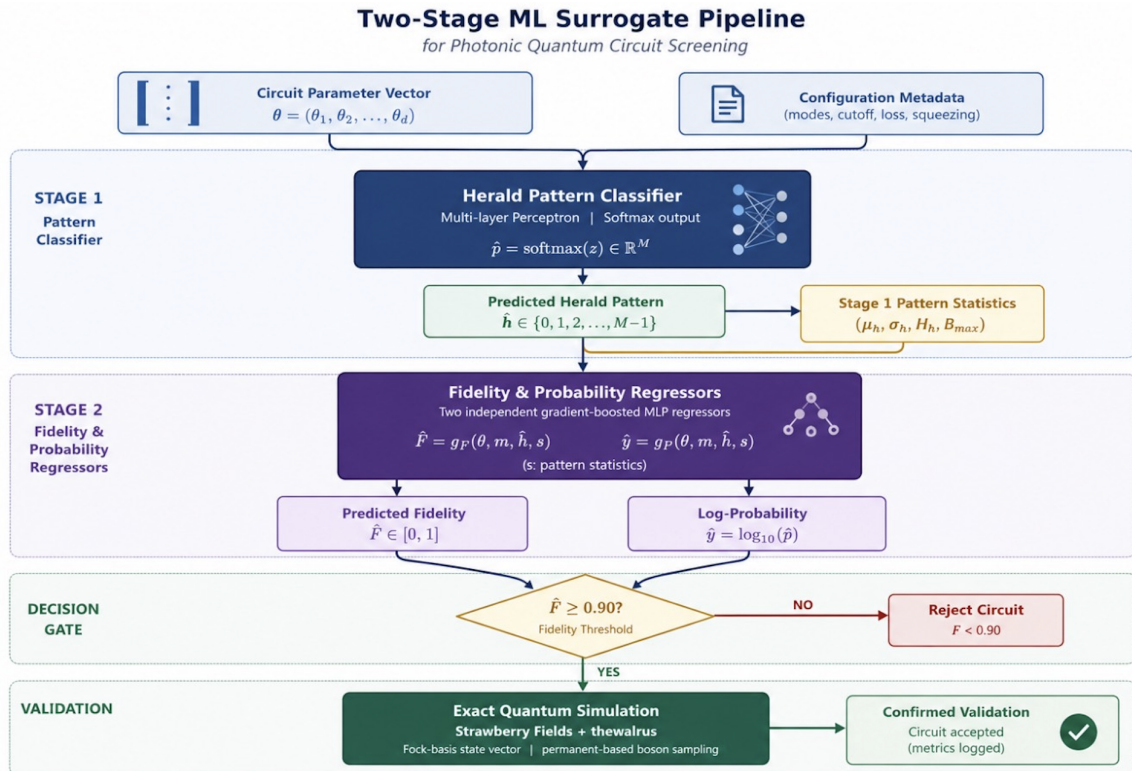


FIG. 2. Two-stage ML surrogate pipeline block diagram. Stage 1 (Pattern Classifier) takes the circuit parameter vector and configuration metadata as input and outputs the predicted herald pattern. Stage 2 (Fidelity and Probability Regressors) takes the same input augmented with the Stage 1 pattern statistics and outputs predicted fidelity F and log-probability $y = \log_{10}(p)$. If $F \geq 0.90$, the circuit is passed to exact quantum simulation (Strawberry Fields + `thewalrus`) for confirmed validation.

B. Dataset Construction

The training dataset was assembled from 423 pickle files generated by running the GKP preparation circuit optimiser derived from the Xanadu approximate-GKP-prep repository [26, 29]. Each pickle file encodes the optimised circuit parameters and corresponding fidelity and probability values for a specific $(n_{\max}, n_{\text{modes}}, \mathbf{m}, \Delta)$ configuration. Circuit configurations span $n_{\text{modes}} \in \{3, 4, 5\}$ optical modes, $n_{\max} \in \{4, 8, 12\}$ Fock-space truncation, and $\Delta \in \{3-11\}$ dB target envelope squeezing.

For each configuration, circuit parameters were optimised in two sequential phases. Phase 1 applied the SLSQP gradient-based minimiser [31] from a randomly sampled starting point to minimise:

$$\mathcal{L}(\boldsymbol{\theta}) = -[F(\boldsymbol{\theta}) + p(\boldsymbol{\theta})], \quad (12)$$

subject to bounds $r_k \in [-r_{\max}, r_{\max}]$ for squeezing amplitudes and $\theta_k, \phi_k \in [-\pi, \pi]$ for all interferometer angles. This cost function equally weights fidelity maximisation and probability maximisation. Phase 2 applied the basin-hopping global optimiser [32] with 50 random jumps and SLSQP as the local minimiser, using a modified cost:

$$\mathcal{L}'(\boldsymbol{\theta}) = -[F(\boldsymbol{\theta}) + 0.1 p(\boldsymbol{\theta})]. \quad (13)$$

The reduced weight on probability in the global phase deliberately deprioritises probability during random exploration, preventing premature convergence into basins characterised by high post-selection probability but low fidelity. Both

the Phase 1 and Phase 2 solutions were retained as separate training samples, yielding two data points per pickle file. From 423 files, this produced 846 samples. An additional 13 benchmark configurations from prior GKP simulation studies (`paper_data`) were included, yielding 859 total samples.

The dataset was partitioned as follows: the 846 `test_data` samples were randomly shuffled (random seed = 42) and split 80/20 into 676 training and 170 test samples. All 13 paper benchmark samples were added to the training partition, giving 689 training samples and 170 holdout samples.

Of the 689 training samples, 457 (66.3%) have fidelity $F \geq 0.90$ and are labelled GKP-capable. This 2:1 imbalance was addressed through explicit sample weighting during model training; paper benchmark circuits received a weight multiplier of $10\times$, anchoring the model on precisely characterised reference configurations; GKP-capable samples received an additional multiplier of $2\times$, improving sensitivity at and near the $F = 0.90$ classification boundary. All weights were normalised to unit mean before training.

C. Feature Engineering

A central design choice in the proposed pipeline is the use of a fixed-dimensional feature representation that accommodates circuits of varying size ($n_{\text{modes}} \in \{3, 4, 5\}$) without requiring separate models for each topology. This is achieved by zero-padding all parameter vectors to match the maximum dimensions in the training set ($\max n_{\text{modes}} = 5$, $\max n_{\text{splitters}} = 10$) and concatenating four categories of descriptors.

The first category consists of raw circuit parameters. The n_{modes} squeezing amplitudes r_k , the $n_{\text{modes}}(n_{\text{modes}} - 1)/2$ beamsplitter mixing angles θ_k , and the beamsplitter phases ϕ_k are each zero-padded to lengths 5, 10, and 10 respectively, producing a 25-element raw parameter block. These features retain full information about the circuit, including the sign of squeezing amplitudes—a property that introduces a systematic failure mode when test circuits use sign conventions underrepresented in training (see Section V). The second category consists of configuration metadata. The scalar values n_{max} , n_{modes} , and Δ are appended directly. These three scalars are among the most physically informative features: the achievable fidelity ceiling is fundamentally constrained by n_{max} (which determines the accuracy of the Fock-basis GKP approximation) and Δ (which sets the target squeezing level). The third category consists of physics-derived aggregate features. Eleven statistics are computed from the raw circuit parameters to encode domain knowledge not directly recoverable from the zero-padded raw features, as defined in Table I.

TABLE I. Physics-derived aggregate features (Category 3).

Feature Name	Definition	Physical Interpretation
<code>total_sq_power</code>	$\sum_k r_k^2$	Total optical squeezing energy injected
<code>max_sq</code>	$\max_k r_k $	Strongest single-mode squeezing
<code>sq_asymmetry</code>	$\max(r_k) - \min(r_k)$	Spread of squeezing across modes
<code>n_negative_sq</code>	$\#\{k : r_k < 0\}$	Number of phase-displaced squeezers
<code>mean_sq_abs</code>	$\langle r_k \rangle$	Average squeezing per mode
<code>mean_coupling</code>	$\langle \theta_k \rangle$	Average interferometer mixing strength
<code>coupling_spread</code>	$\sigma(\theta_k)$	Uniformity of beamsplitter coupling
<code>phase_coherence</code>	$\sigma(\phi_k)$	Spread of interferometer phases
<code>near_pi_count</code>	$\#\{k : \phi_k - \pi < 0.1\}$	Number of near- π phase rotations
<code>nmax_per_mode</code>	$n_{\text{max}}/n_{\text{modes}}$	Effective photons per mode
<code>delta_over_nmax</code>	Δ/n_{max}	Squeezing quality per Fock level

Note that `total_sq_power`, `max_sq`, `mean_sq_abs`, and `sq_asymmetry` are sign-invariant in magnitude. However, the raw squeezing parameters in Category 1 are sign-sensitive. This asymmetry—partially sign-invariant physics features combined with sign-sensitive raw parameters—is the root cause of the failure mode documented in Section V. Note also that `near_pi_count` counts phases close to $\pm\pi$ in absolute value (i.e. $||\phi_k| - \pi| < 0.1$), capturing the physical near-equivalence of $+\pi$ and $-\pi$ phases for the beamsplitter gate.

The final category consists of Herald pattern statistics (Stage 2 only). Eight statistics summarising the herald pattern structure are appended to the Stage 2 feature vector: `pat_sum` = $\sum_i m_i$ (always equals n_{max}), `pat_len` = $n_{\text{modes}} - 1$, and `pat_max`, `pat_min`, `pat_mean`, `pat_std`, `pat_median`, `pat_range`. These allow Stage 2 to condition its predictions on the photon-count distribution being post-selected.

All features in both Stage 1 and Stage 2 vectors were standardised to zero mean and unit variance using `sklearn StandardScaler` [33] fitted exclusively on the training set. Two independent scalers were maintained—one for the Stage 1 feature vector (Categories 1–3, dimension 39) and one for the Stage 2 feature vector (Categories 1–4, dimension 47)—preventing data leakage between splits and inconsistency in normalisation between pipeline stages.

D. Model Architecture and Cascade Design Rationale

The three prediction targets—optimal herald pattern, circuit fidelity, and post-selection probability—are not independent. The fidelity and probability achievable by a circuit depend on which herald pattern is applied: different patterns probe different photon-number correlations in the multimode state, and the pattern that maximises fidelity is not always the one that maximises probability. The cascade design propagates the Stage 1 pattern prediction as a feature into Stage 2, allowing the fidelity and probability regressors to exploit the physical relationship between pattern geometry and circuit performance.

Stage 1: Herald Pattern Classifier. A `HistGradientBoostingClassifier` [33, 34] is trained on the Stage 1 feature vector (39 features) to predict the optimal herald pattern as a multiclass label. Herald patterns are represented as ampersand-delimited strings (e.g., "3&5" for pattern [3, 5]) and mapped to integer class labels via `LabelEncoder`. For circuit configurations whose predicted pattern falls outside the set of mathematically valid patterns for the given $(n_{\max}, n_{\text{modes}})$, a nearest-neighbour correction maps the prediction to the closest valid pattern by Euclidean distance. Hyperparameters for the multiclass case (more than two valid patterns): `max_iter` = 500, `max_depth` = 8, `learning_rate` = 0.05, `min_samples_leaf` = 3, `l2_regularization` = 0.1. For the binary case (exactly two valid patterns): `max_iter` = 300, `max_depth` = 6, `learning_rate` = 0.05.

Stage 2a: Fidelity Regressor. A `HistGradientBoostingRegressor` is trained on the Stage 2 feature vector (47 features, where Category 4 contains the statistics of the Stage 1 predicted pattern) to predict circuit fidelity $F \in [0, 1]$. Predictions are clipped to $[0, 1]$ at inference. The GKP-capability threshold $F \geq 0.90$ applied to the Stage 2a output is the primary classification gate. Hyperparameters: `max_iter` = 500, `max_depth` = 8, `learning_rate` = 0.05, `min_samples_leaf` = 5, `l2_regularization` = 0.1.

Stage 2b: Probability Regressor. A second `HistGradientBoostingRegressor` predicts the log-transformed post-selection probability:

$$y = \log_{10}(p + \varepsilon), \quad \varepsilon = 10^{-30}, \quad (14)$$

where the offset ε prevents undefined logarithms for configurations with numerically zero post-selection probability. Predictions are back-transformed at inference via $p = 10^y$ and clipped to $[0, 1]$. The log transformation is essential: the raw probability spans approximately ten orders of magnitude across the training set (from $\sim 10^{-12}$ to $\sim 10^{-2}$), and regressing on untransformed values would cause the MSE loss to be dominated by the small number of high-probability configurations. In \log_{10} scale, an MAE of 1.0 corresponds to exactly one order of magnitude error—a natural and interpretable unit given the observed dynamic range. Hyperparameters: identical to Stage 2a.

E. Conditional Validation Architecture

The surrogate pipeline does not make final predictions autonomously. Instead, it implements a conditional validation structure in which exact quantum simulation is triggered for every circuit that passes the surrogate screening gate (predicted $F \geq 0.90$). Specifically:

- (i) The full GBS circuit is simulated using the Strawberry Fields Gaussian backend, which propagates the circuit covariance matrix Σ and displacement vector $\boldsymbol{\mu}$ analytically through all squeezing and interferometer stages.
- (ii) The post-selection probability is computed using `density_matrix_element` from `thewalrus`, which evaluates the hafnian of the relevant covariance submatrix.
- (iii) The heralded state is extracted using `state_vector` (lossless) or `density_matrix` (lossy) from `thewalrus`.
- (iv) The fidelity between the heralded state and the target GKP Fock-basis representation is computed exactly.
- (v) The Wigner function is evaluated on a 100×100 phase-space grid over $q, p \in [-7, 7]$ using an iterative algorithm adapted from QuTiP, and Wigner log-negativity is computed on a separate 200×200 grid by 2D numerical integration using `scipy.integrate.simpson`.
- (vi) Simulation results (fidelity, probability, Wigner function, WLN) are returned alongside the surrogate predictions and presented side by side.

This architecture means the surrogate serves exclusively as a computational filter, not as the final authority on circuit performance. False-positive surrogate predictions are exposed immediately by the subsequent simulation. False-negative predictions—GKP-capable circuits rejected by the surrogate—are the true cost of the screening step, representing circuits never simulated and thus never discovered. For large circuits ($n_{\max} = 12$, five modes) where each

(circuit, pattern) evaluation costs approximately five minutes and up to 15 valid patterns exist, exhaustive screening of 10,000 candidates would require approximately 12,500 CPU-hours. Restricting full simulation to only the 10% of surrogate-endorsed candidates reduces this to approximately 1,250 CPU-hours—a tenfold reduction—with the surrogate’s pattern recommendation eliminating the need to evaluate all 15 patterns per approved circuit.

IV. QUANTITATIVE EVALUATION

Any honest assessment of a binary classifier requires comparison against trivial baselines. For the GKP-detection task, two natural baselines exist. The majority-class baseline—always predicting “GKP-capable”—achieves accuracy equal to the GKP-capable fraction: $457/689 = 66.3\%$ on the training set, approximately 66.3% on the holdout. The random baseline—predicting “GKP-capable” with probability equal to the training class frequency—achieves approximately $66.3^2 + 33.7^2 \approx 55\%$.

The surrogate pipeline achieves 90.0% GKP-detection accuracy on the holdout set, representing a 23.7 percentage-point improvement over the majority-class baseline—a meaningful and non-trivial result. However, this must be read in context: 10% of holdout circuits are incorrectly classified, of which some fraction are false positives (GKP-incapable circuits passed to simulation) and the remainder are false negatives (GKP-capable circuits rejected).

For the pattern classifier, the 64.0% cross-validated accuracy represents a meaningful improvement over chance (which ranges from 6.7% for 15-class configurations to 50% for 2-class configurations). However, the 36% error rate in Stage 1 propagates into Stage 2 feature errors with consequences for fidelity prediction quality that are discussed further in Section VI.

Table II contextualises the surrogate’s GKP-detection accuracy against trivial baselines on the holdout set. Table III presents all quantitative performance metrics across training, cross-validation (5-fold), and holdout evaluation.

TABLE II. GKP-detection accuracy of the surrogate pipeline against trivial baselines on the held-out test set ($n = 170$). The majority-class baseline always predicts “GKP-capable” and achieves the training-set class frequency ($457/689 = 66.3\%$); the random baseline predicts “GKP-capable” with that same probability, yielding $66.3^2 + 33.7^2 \approx 55\%$. Wilson-score 95 % confidence intervals are reported for the surrogate only, since the baselines are deterministic thresholds rather than stochastic predictors evaluated on the holdout. pp = percentage points.

Method	Accuracy	95 % CI	Δ vs. majority
Random baseline	$\approx 55.0\%$	—	−11.3 pp
Majority-class baseline	66.3%	—	—
Surrogate (ours)	90.0%	[84.8%, 93.6%]	+23.7 pp

TABLE III. Complete quantitative performance metrics across all pipeline stages.

Model	Metric	CV Score	CV $\pm 2\sigma$	Holdout
Pattern Classifier	Accuracy	0.640	± 0.067	—
Fidelity Regressor	R^2	0.689	± 0.294	0.760
Fidelity Regressor	MAE	—	—	0.032
Probability Regressor	R^2 (\log_{10})	0.811	± 0.138	0.837
Probability Regressor	MAE (\log_{10})	—	—	0.432
GKP Detection	Accuracy	—	—	0.900
Majority-class baseline	Accuracy	—	—	≈ 0.663
Improvement	Δ Accuracy	—	—	+0.237

Fidelity regressor performance. The holdout R^2 of 0.760 indicates the model explains approximately 76% of fidelity variance across the 170 holdout configurations. The MAE of 0.032 is the more practically useful metric: fidelity predictions deviate from exact simulation by an average of 3.2 percentage points. This is acceptable for circuits well above or well below $F = 0.90$, but is imprecise for circuits near the threshold.

The cross-validation R^2 of 0.689 ± 0.294 warrants serious attention. The 2σ spread means individual fold R^2 values may range from approximately 0.40 to 0.98. A fold R^2 of 0.40 implies that in some subsets of the parameter space, the model explains less than half the fidelity variance—approaching the performance of a simple mean predictor.

Probability regressor performance. The holdout log-scale R^2 of 0.837 and MAE of 0.432 indicate the model predicts post-selection probabilities to within approximately half an order of magnitude on average. Given that

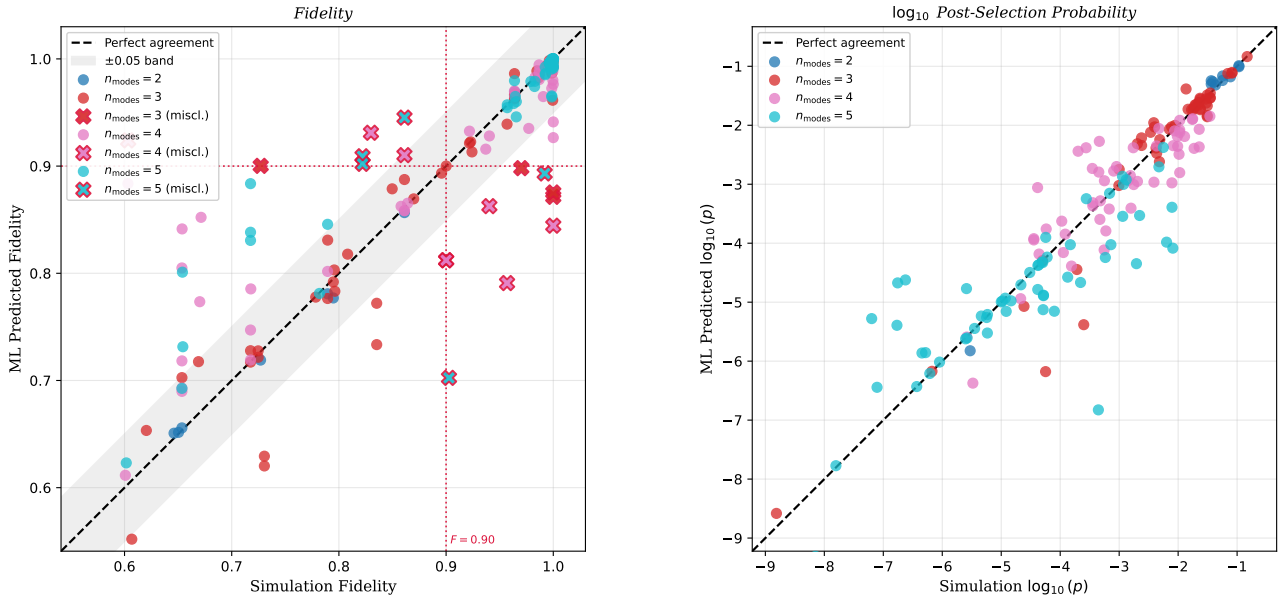
Figure 3. ML-Predicted vs Simulation-Confirmed — Holdout Set (170 samples)


FIG. 3. Scatter plot of ML-predicted vs. simulation-confirmed fidelity (left) and \log_{10} post-selection probability (right) on the 170-sample holdout set. Points are coloured by circuit mode count ($n_{\text{modes}} \in \{3, 4, 5\}$). The dashed diagonal line indicates perfect agreement. The shaded band indicates ± 0.05 fidelity error. Points above or below the $F = 0.90$ threshold line that are misclassified by the surrogate are highlighted.

probabilities span ten orders of magnitude across the dataset, this is a useful level of accuracy for experimental resource planning—reliable discrimination between circuits requiring minutes versus hours of data collection—but should not be used for precise rate estimation in experiments requiring narrow probability windows.

Paper benchmark results. The 13 paper benchmark circuits achieve $R^2 = 1.00$ and $\text{MAE} \approx 0.000$ for both fidelity and probability. This result must be interpreted cautiously: these circuits received a $10\times$ training weight, effectively forcing the model to reproduce their values through local interpolation. This is evidence of memorisation of heavily-weighted training points, not of strong out-of-distribution generalisation.

Cascade vulnerability. The 36% Stage 1 pattern misclassification rate means Stage 2 receives incorrect pattern statistics as input in approximately one third of cases. The aggregate holdout MAE of 0.032 mixes correctly-conditioned Stage 2 predictions ($\approx 64\%$ of cases) with incorrectly-conditioned ones ($\approx 36\%$), potentially obscuring much larger errors in the misclassified subset.

V. CASE STUDIES: SURROGATE PREDICTION VS. EXACT SIMULATION

Nine circuit configurations were selected to characterise the pipeline’s end-to-end behaviour across a range of mode counts, Fock truncations, and squeezing targets. These circuits were deliberately chosen—not randomly sampled—to span diverse configurations: the paper demo circuit (C1), configurations at both ends of the n_{max} range (C6 at $n_{\text{max}} = 4$; F1 at $n_{\text{max}} = 12$), and configurations designed to explore the sign-sensitivity failure mode (C3 vs. F1; C4 vs. F2).

For each circuit, the pipeline executed the following sequence: Stage 1 predicted the optimal herald pattern; Stage 2 predicted fidelity and probability conditional on the Stage 1 pattern; if $F \geq 0.90$, exact Strawberry Fields simulation was performed; the Wigner function was computed and Wigner log-negativity evaluated numerically; surrogate predictions and simulation results were compared.

Table IV summarises all nine circuits. Circuits C1–C7 are successful predictions; F1 and F2 are systematic failure cases.

Pattern recommendation. The surrogate correctly recommended the herald pattern in all seven successful cases. This is the most operationally important correct prediction: an incorrect pattern recommendation not only conditions Stage 2 poorly but directs the subsequent simulation to the wrong post-selection, guaranteeing a wrong fidelity result even if exact simulation is performed.

TABLE IV. End-to-end case study results. \checkmark indicates correct pattern recommendation. Rows F1 and F2 are failure cases. $\Delta F = |F_{\text{ML}} - F_{\text{sim}}|$ is the absolute fidelity prediction error.

Config	$n_{\text{max}}/n_{\text{modes}}/\Delta$ (dB)	Pattern	F_{ML}	F_{sim}	ΔF	p_{ML}	p_{sim}	WLN
C1 (demo)	8/3/10	[4, 4] \checkmark	0.969	0.999	0.030	4.22×10^{-3}	4.10×10^{-3}	0.700
C2	8/4/5	[2, 3, 3] \checkmark	0.971	0.971	0.001	9.20×10^{-13}	8.67×10^{-13}	0.115
C3	12/5/11 (-)	[1, 2, 3, 6] \checkmark	1.000	0.999	0.000	1.89×10^{-5}	1.89×10^{-5}	0.736
C4	12/4/10 (+)	[3, 4, 5] \checkmark	0.956	0.980	0.025	8.95×10^{-7}	8.96×10^{-7}	0.700
C5	8/4/10	[2, 2, 4] \checkmark	1.000	1.000	0.000	1.35×10^{-3}	1.36×10^{-3}	0.696
C6	4/3/11	[2, 2] \checkmark	0.999	0.999	0.001	1.57×10^{-2}	1.54×10^{-2}	0.640
C7	8/3/5	[3, 5] \checkmark	0.964	0.965	0.002	3.30×10^{-2}	3.50×10^{-2}	0.022
F1 \times	12/5/11 (+)	[1, 2, 3, 6] \checkmark	0.995	0.307	0.688	1.36×10^{-5}	7.81×10^{-5}	0.518
F2 \times	12/4/10 (-)	[3, 4, 5] \checkmark	0.929	0.001	0.928	2.50×10^{-6}	1.93×10^{-5}	0.563

Fidelity agreement. Fidelity prediction errors range from essentially zero (C2: $\Delta F = 0.001$; C3: $\Delta F \approx 0$; C5: $\Delta F \approx 0$) to a maximum of $\Delta F = 0.030$ for C1 (the paper demo circuit). This 3 percentage-point underestimation does not constitute a classification error—both values are well above 0.90—but illustrates that the surrogate can be systematically conservative for high-fidelity circuits.

Probability agreement. Post-selection probability predictions span many orders of magnitude: from 9.20×10^{-13} for C2 to 3.30×10^{-2} for C7. Despite this range, surrogate and simulation agree closely in most cases—C3 achieves near-exact agreement and C4 achieves agreement to four significant figures.

Wigner log-negativity and the fidelity-only threshold problem. The WLN values reveal a significant limitation of $F \geq 0.90$ as the sole quality criterion. C2 (WLN = 0.115) and C7 (WLN = 0.022) both satisfy the fidelity threshold but have WLN values approaching zero—a state with WLN ≈ 0 is essentially classically simulable and cannot provide quantum computational advantage for non-Clifford gate synthesis or magic state distillation [27]. This is not a failure of the surrogate, which makes no WLN predictions; it is a limitation of the threshold criterion itself. The WLN pattern is physically interpretable: WLN correlates with both Δ and n_{max} . Lower Δ (e.g., 5 dB for C7) produces a less squeezed finite-energy approximation with weaker negativity and lower WLN. Higher Δ (e.g., 10–11 dB for C1, C4, C5) produces sharper phase-space peaks, stronger negativity, and WLN consistently in the range 0.63–0.74.

Systematic failure cases F1 and F2. The surrogate predicts $F = 0.995$ for F1 and $F = 0.929$ for F2. Exact simulation reveals $F_{\text{sim}} = 0.307$ for F1 and $F_{\text{sim}} = 0.001$ for F2—errors of $\Delta F = 0.688$ and $\Delta F = 0.928$ respectively. Without the mandatory simulation validation step, these circuits would be incorrectly endorsed as high-quality GKP state generators. The source of this failure is identifiable through controlled comparison:

F1 uses squeezing parameters $[+1.701, -0.254, -0.711, -1.724, -1.725]$ (predominantly positive first parameter) with configuration ($n_{\text{max}} = 12, n_{\text{modes}} = 5, \Delta = 11$ dB, $\mathbf{m} = [1, 2, 3, 6]$). C3 uses squeezing parameters $[-1.701, -0.254, -0.711, -1.724, -1.725]$ —the same magnitudes, negated first parameter—with identical configuration. F1 yields $F_{\text{sim}} = 0.307$; C3 yields $F_{\text{sim}} = 0.999$. The surrogate predicts $F = 0.995$ for F1 and $F = 0.9995$ for C3—near-identical surrogate predictions for circuits whose actual fidelities differ by more than 0.69. The same pattern holds for F2 vs. C4.

This is not a random error. It is a systematic consequence of the training data’s sign distribution: the optimised configurations apparently cluster more heavily in one sign convention for five-mode and four-mode circuits with high n_{max} . When a test circuit falls in the underrepresented sign convention, the surrogate maps it to a high-fidelity training neighbourhood that does not correspond to its actual physical behaviour. The conditional simulation step prevents these failures from propagating: both F1 and F2 trigger exact simulation, which immediately reveals the true fidelities. The surrogate fails; the pipeline does not.

VI. DISCUSSION

For circuit configurations within the training distribution—specifically 3–5 mode GBS circuits with $n_{\text{modes}} \in \{3, 4, 5\}$, $n_{\text{max}} \in \{4, 8, 12\}$, and $\Delta \in \{3\text{--}11\}$ dB—the proposed surrogate achieves reliable performance in identifying GKP-capable circuits, reaching an accuracy of approximately 90%, corresponding to a 23.7 percentage-point improvement over the baseline. Within successfully validated cases, it correctly identifies suitable heralding patterns and predicts circuit fidelity with a mean absolute error of 0.032. These outputs are produced in the millisecond regime, and any circuit that satisfies the GKP threshold is immediately subjected to full exact quantum simulation for verification.

However, the surrogate does not generalise robustly beyond the training distribution. This limitation is primarily manifested through a sign-sensitivity failure mode, where deviations in squeezing-parameter conventions lead to

GKP State Wigner Function [pattern 4&4]
 Sim fidelity = 0.9985 Prob = 4.10e-03 WLN = 0.7000

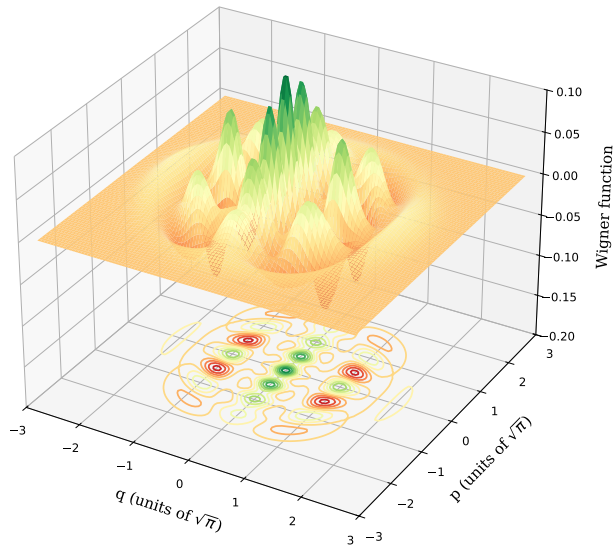


FIG. 4. Representative Wigner functions $W(q, p)$ from the exact simulation step, plotted over $q, p \in [-3, 3]$ (in units of $\sqrt{\pi}$). **(a)** Circuit C1 ($n_{\max} = 8$, three modes, $\Delta = 10$ dB, WLN = 0.700): characteristic GKP lattice structure with prominent negativity (red/blue regions) at phase-space lattice points. **(b)** Circuit C7 ($n_{\max} = 8$, three modes, $\Delta = 5$ dB, WLN = 0.022): the GKP pattern is visually present but with negligible negativity, consistent with near-classical behaviour. **(c)** Circuit F1 ($n_{\max} = 12$, five modes, $\Delta = 11$ dB, sign +): the Wigner function bears no resemblance to a GKP state, consistent with $F_{\text{sim}} = 0.307$, confirming the catastrophic surrogate failure.

degraded predictions. In addition, the model does not directly predict Wigner logarithmic negativity (WLN), and its fidelity regressor exhibits non-uniform performance across the parameter space, with cross-validated R^2 values decreasing to approximately 0.40 in certain regimes. Furthermore, the Stage 1 pattern classifier, with an accuracy of around 64%, introduces cascading errors that propagate into Stage 2 predictions and are not fully captured by aggregate metrics.

A key aspect of the framework is that it does not function as a standalone predictor. Instead, it operates as a computational filter: every circuit predicted to be GKP-capable is subsequently validated via exact quantum simulation, ensuring that reported fidelity, success probability, and Wigner-logarithmic-negativity values are physically grounded and independent of surrogate error. This separation between fast inference and exact verification is essential for maintaining reliability in practice.

Several limitations remain. First, the sign-sensitivity issue can be mitigated through symmetry-augmented training data, sign-invariant feature construction, or explicit input canonicalisation to enforce consistent parameter conventions. Second, the observed cross-validation variability ($R^2 = 0.689 \pm 0.294$) suggests heterogeneous model reliability, which could be improved through active learning strategies [35] that prioritise simulation in high-uncertainty regions. Third, the cascade vulnerability introduced by Stage 1 misclassification can be addressed either by improving training coverage in high-degeneracy regimes or by removing hard conditioning and allowing Stage 2 to model all valid herald patterns jointly. Finally, the absence of WLN prediction limits the ability to directly screen for non-classical computational utility; incorporating WLN as an additional regression target would extend the model beyond fidelity estimation.

From a computational perspective, the advantage of the surrogate is substantial. For five-mode circuits with $n_{\max} = 12$, each circuit-pattern evaluation requires approximately five minutes using exact methods, and with up to 15 valid herald patterns this results in roughly 75 minutes per circuit. By contrast, the surrogate produces predictions in approximately 1–5 ms, yielding speedups on the order of 10^5 for large configurations. In large-scale screening scenarios [3], where approximately 90% of candidates are rejected prior to simulation, the total computational cost for evaluating 10,000 circuits is reduced from approximately 12,500 CPU-hours under exhaustive evaluation to about 1,250 CPU-hours under surrogate-guided filtering.

Finally, the reliability of the framework is strictly bounded by its training distribution. It is trained on $n_{\text{modes}} \in \{3, 4, 5\}$, $n_{\max} \in \{4, 8, 12\}$, and $\Delta \in \{3-11\}$ dB, and performance degrades outside these ranges, including for different mode counts, higher Fock truncations, or alternative squeezing regimes. In such cases, full quantum simulation remains the only dependable evaluation method.

VII. CONCLUSION

We have presented a two-stage gradient-boosted surrogate pipeline for rapid screening of GBS circuits targeting GKP state generation. Trained on 689 circuit configurations across 3–5 optical modes, the surrogate achieves 90.0% GKP-detection accuracy on a held-out set—a 23.7 percentage-point improvement over the majority-class baseline—with fidelity MAE of 0.032 and log-scale post-selection $R^2 = 0.837$. For the most computationally demanding configurations ($n_{\max} = 12$, five modes), this reduces a ten-thousand-circuit search from $\approx 12,500$ CPU-hours to $\approx 1,250$: a tenfold acceleration that makes large-scale parameter exploration practical.

The surrogate has clearly defined limits. Cross-validation fidelity $R^2 = 0.689 \pm 0.294$ reveals heterogeneous reliability, and the 36% Stage 1 misclassification rate compounds into Stage 2 errors that aggregate metrics understate. Out-of-distribution squeezing conventions cause fidelity errors up to $\Delta F = 0.928$, which are caught and contained by the mandatory exact simulation step—the essential reliability guarantee that separates the system from an autonomous predictor.

Three improvements would close the remaining gaps: symmetry-augmented training to resolve sign-convention sensitivity; active learning to reduce cross-validation variance; and the addition of Wigner logarithmic negativity as a regression target. These extensions would move the pipeline toward a fully reliable surrogate for autonomous GKP circuit design confirmed by quantum simulation.

CREDIT AUTHORSHIP CONTRIBUTION STATEMENT

All authors had an equal and shared role in all stages of the research, including conceptualization, study design, data collection and analysis, writing, and revision of the manuscript.

DECLARATION OF COMPETING INTEREST

The authors confirm that there are no known competing financial interests or personal relationships that could have influenced the work reported in this paper.

DATA AVAILABILITY

The data that support the findings of this study are available from the corresponding author upon reasonable request.

REFERENCES

-
- [1] Michael A. Nielsen and Isaac L. Chuang. *Quantum Computation and Quantum Information*. Cambridge University Press, 2000.
- [2] Fulvio Flamini, Nicolò Spagnolo, and Fabio Sciarrino. Photonic quantum information processing: a review. *Reports on Progress in Physics*, 82:016001, 2019.
- [3] J. Eli Bourassa, Rafael N. Alexander, Michael Vasmer, Ashlesha Patil, Ilan Tzitrin, Takaya Matsuura, Daiqin Su, Ben Q. Baragiola, Saikat Guha, Guillaume Dauphinais, Krishna K. Sabapathy, Nicolas C. Menicucci, and Ish Dhand. Blueprint for a scalable photonic fault-tolerant quantum computer. *Quantum*, 5:392, 2021.
- [4] Daniel Gottesman, Alexei Kitaev, and John Preskill. Encoding a qubit in an oscillator. *Physical Review A*, 64:012310, 2001.
- [5] Scott Glancy and Emmanuel Knill. Error analysis for encoding a qubit in an oscillator. *Physical Review A*, 73:012325, 2006.
- [6] Barbara M. Terhal, Jeremy Conrad, and Christophe Vuillot. Towards scalable bosonic quantum error correction. *Quantum Science and Technology*, 5:043001, 2020.
- [7] Ilan Tzitrin, Takaya Matsuura, Rafael N. Alexander, Guillaume Dauphinais, J. Eli Bourassa, Krishna K. Sabapathy, Nicolas C. Menicucci, and Ish Dhand. Fault-tolerant quantum computation with static linear optics. *PRX Quantum*, 2:040353, 2021.
- [8] Kyungjoo Noh, Christopher Chamberland, and Fernando G. S. L. Brandão. Low-overhead fault-tolerant quantum error correction with the surface-gkp code. *PRX Quantum*, 3:010315, 2022.
- [9] Philippe et al. Campagne-Ibarcq. Quantum error correction of a qubit encoded in grid states of an oscillator. *Nature*, 584:368–372, 2020.
- [10] Christoph et al. Flühmann. Encoding a qubit in a trapped-ion mechanical oscillator. *Nature*, 566:513–517, 2019.
- [11] V. V. Sivak, A. Eickbusch, B. Royer, S. Singh, I. Tsioutsios, S. Ganjam, A. Miano, B. L. Brock, A. Z. Ding, L. Frunzio, S. M. Girvin, R. J. Schoelkopf, and M. H. Devoret. Real-time quantum error correction beyond break-even. *Nature*, 616:50–55, 2023.
- [12] Julien Etesse, Matthieu Bouillard, Bharat Kanseri, and Rosa Tualle-Broui. Experimental generation of squeezed cat states with an operation allowing iterative growth. *Physical Review Letters*, 114:193602, 2015.
- [13] Miller Eaton, Rajveer Nehra, and Olivier Pfister. Non-Gaussian and Gottesman–Kitaev–Preskill state preparation by photon catalysis. *New Journal of Physics*, 21:113034, 2019.
- [14] David J. Weigand and Barbara M. Terhal. Generating grid states from schrödinger-cat states without postselection. *Physical Review A*, 97:022341, 2018.
- [15] Austin P. Lund, Andrew Laing, Saleh Rahimi-Keshari, Terry Rudolph, Jeremy L. O’Brien, and Timothy C. Ralph. Boson sampling from a gaussian state. *Physical Review Letters*, 113:100502, 2014.
- [16] Craig S. Hamilton, Regina Kruse, Linda Sansoni, Sonja Barkhofen, Christine Silberhorn, and Igor Jex. Gaussian boson sampling. *Physical Review Letters*, 119:170501, 2017.
- [17] Han-Sen Zhong, Hui Wang, Yu-Hao Deng, Ming-Cheng Chen, Li-Chao Peng, Yi-Han Luo, Jian Qin, Dian Wu, Xing Ding, Yi Hu, Peng Hu, Xiao-Yan Yang, Wei-Jun Zhang, Hao Li, Yuxuan Li, Xiao Jiang, Lin Gan, Guangwen Yang, Lixing You, Zhen Wang, Li Li, Nai-Le Liu, Chao-Yang Lu, and Jian-Wei Pan. Quantum computational advantage using photons. *Science*, 370:1460–1463, 2020.
- [18] Lars S. Madsen, Fabian Laudenbach, Mohsen Falamarzi Askarani, Fabien Rortais, Trevor Vincent, Jacob F. F. Bulmer, Filippo M. Miatto, Leonhard Neuhaus, Lukas G. Helt, Matthew J. Collins, Adriana E. Lita, Thomas Gerrits, Sae Woo Nam, Varun D. Vaidya, Matteo Menotti, Ish Dhand, Zachary Vernon, Nicolás Quesada, and Jonathan Lavoie. Quantum computational advantage with a programmable photonic processor. *Nature*, 606:75–81, 2022.
- [19] Scott Aaronson and Alex Arkhipov. The computational complexity of linear optics. In *Proceedings of the 43rd Annual ACM Symposium on Theory of Computing*, pages 333–342, 2011.
- [20] Brajesh Gupta, Josh Izaac, and Nicolás Quesada. The walrus: a library for the calculation of hafnians, hermite polynomials and gaussian boson sampling. *Journal of Open Source Software*, 4:1705, 2019.
- [21] Ryan Shaffer, Lucas Kocia, and Mohan Sarovar. Surrogate-based optimization for variational quantum algorithms. *Physical Review A*, 107:032415, 2023.
- [22] Nathan Killoran, Josh Izaac, Nicolás Quesada, Ville Bergholm, Matthew Amy, and Christian Weedbrook. Strawberry fields: A software platform for photonic quantum computing. *Quantum*, 3:129, 2019.
- [23] Arne L. Grimsmo and Shruti Puri. Quantum error correction with the Gottesman–Kitaev–Preskill code. *PRX Quantum*, 2:020101, 2021.
- [24] Kasper Duivenvoorden, Barbara M. Terhal, and David Weigand. Single-mode displacement sensor. *Physical Review A*, 95:012305, 2017.
- [25] Baptiste Royer, Shraddha Singh, and S. M. Girvin. Stabilization of finite-energy Gottesman–Kitaev–Preskill states. *Physical Review Letters*, 125:260509, 2020.
- [26] Ilan Tzitrin, J. Eli Bourassa, Nicolas C. Menicucci, and Krishna Kumar Sabapathy. Progress towards practical qubit computation using approximate Gottesman–Kitaev–Preskill codes. *Physical Review A*, 101:032315, 2020.

- [27] André Kenfack and Karol Życzkowski. Negativity of the wigner function as an indicator of non-classicality. *Journal of Optics B: Quantum and Semiclassical Optics*, 6:396–404, 2004.
- [28] Regina Kruse, Craig S. Hamilton, Linda Sansoni, Sonja Barkhofen, Christine Silberhorn, and Igor Jex. Detailed study of Gaussian boson sampling. *Physical Review A*, 100:032326, 2019.
- [29] Xanadu AI. approximate-gkp-prep: Gkp state generation via gaussian boson sampling, 2024.
- [30] William R. Clements, Peter C. Humphreys, Benjamin J. Metcalf, W. Steven Kolthammer, and Ian A. Walmsley. Optimal design for universal multiport interferometers. *Optica*, 3:1460–1465, 2016.
- [31] Pauli Virtanen, Ralf Gommers, Travis E. Oliphant, Matt Haberland, Tyler Reddy, David Cournapeau, Evgeni Burovski, Pearu Peterson, Warren Weckesser, Jonathan Bright, Stéfan J. van der Walt, Matthew Brett, Joshua Wilson, K. Jarrod Millman, Nikolay Mayorov, Andrew R. J. Nelson, Eric Jones, Robert Kern, Eric Larson, C. J. Carey, İlhan Polat, Yu Feng, Eric W. Moore, Jake VanderPlas, Denis Laxalde, Josef Perktold, Robert Cimrman, Ian Henriksen, E. A. Quintero, Charles R. Harris, Anne M. Archibald, Antônio H. Ribeiro, Fabian Pedregosa, and Paul van Mulbregt. SciPy 1.0: Fundamental algorithms for scientific computing in Python. *Nature Methods*, 17:261–272, 2020.
- [32] David J. Wales and Jonathan P. K. Doye. Global optimization by basin-hopping and the lowest energy structures of Lennard-Jones clusters containing up to 110 atoms. *Journal of Physical Chemistry A*, 101:5111–5116, 1997.
- [33] Fabian Pedregosa, Gaël Varoquaux, Alexandre Gramfort, Vincent Michel, Bertrand Thirion, Olivier Grisel, Mathieu Blondel, Peter Prettenhofer, Ron Weiss, Vincent Dubourg, Jake Vanderplas, Alexandre Passos, David Cournapeau, Matthieu Brucher, Matthieu Perrot, and Edouard Duchesnay. Scikit-learn: Machine learning in Python. *Journal of Machine Learning Research*, 12:2825–2830, 2011.
- [34] Jerome H. Friedman. Greedy function approximation: A gradient boosting machine. *Annals of Statistics*, 29:1189–1232, 2001.
- [35] Burr Settles. *Active Learning*. Synthesis Lectures on Artificial Intelligence and Machine Learning. Morgan & Claypool Publishers, 2012.